Journal of MATERIALS RESEARCH

Article
DOI:10.1557/s43578-022-00763-3

Dielectric breakdown of heterogeneous materials under electromagnetic pulses

Ju Hwan Shin[1], Daniel Olsen[1], Christopher Coffelt[1], Luis San Martin[3], Min Zhou[1,2,a)]

[1] The George W. Woodruff School of Mechanical Engineering, Georgia Institute of Technology, Atlanta, GA 30332-0405, USA
[2] School of Materials Science and Engineering, Georgia Institute of Technology, Atlanta, GA 30332-0405, USA
[3] Sandia National Laboratories, Albuquerque, NM 87185, USA
[a)] Address all correspondence to this author. e-mail: min.zhou@gatech.edu

Received: 29 March 2022; accepted: 26 September 2022; published online: 13 October 2022

Microstructure models are developed to computationally analyze the interactions between the constituents in heterogeneous materials and electromagnetic pulses (EMP). The models are used to explicitly simulate the material breakdown process by tracking the transition of dielectric constituents from non-conductive to conductive states. The focus is on the electric fields induced in the materials and the conditions for dielectric breakdown (defined as the onset of avalanche) caused by an artificially induced EMP excitation. The materials analyzed contain different combinations of dielectric and conductive constituents, a material made of cellulose-based KRAFT paper and mineral oil, PEEK 450G, and a gasket material (Parker Chomerics 1287). It is found that the electric field levels in the materials and the breakdown behavior are significantly affected by microstructure heterogeneities. The breakdown strengths of these materials depend on the microstructures, the dielectric constants, breakdown strengths, and the post-breakdown conductivity of the constituents.

Introduction

Electromagnetic pulse (EMP) wave interaction with both conductive and non-conductive materials has been of scientific interest for the better part of the past century. With the advent of nuclear weapons in the 1940s, EMP effects were quickly identified as a dangerous byproduct of nuclear detonation [1]. Other naturally occurring phenomena are also capable of producing these effects, such as lightning and geomagnetic storms caused by solar flares [2–4]. The artificially produced EMP events can have three distinct components, E1, E2, and E3. The component investigated in this research is E1, which can be characterized by a sharp peak that can last up to a few nanoseconds prior to decaying. E1 pulses are particularly damaging to the circuitry in computers and electronics devices, as the voltages and the induced currents happen too quickly for traditional surge protection to function properly. The sharp peak can also cause large voltages in non-conductive materials and high currents in conductors. The high voltages and high currents can cause damage to the insulation material, sensitive materials adjacent to it, semiconductors, and conductors.

The damage to insulators and semiconductors occur via dielectric breakdown in which the material becomes conductive. The damage to conducting materials is via high voltages and currents. Microscopically, most materials are heterogeneous due to the presence of different constituents, complicated constituent morphologies and sizes, and defects such as voids, cracks, and interfaces. The heterogeneities cause the local electric field (E-field) conditions to be magnified relative to the macroscopic incoming field conditions, thereby significantly increasing the likelihood of material damage and failure. Sun et al. [5] added periodic and random sets of circular inclusions to study the effect on the electric field, where the randomness of the particles not only affected the local increase in electric field but also the energy transmitted by the material. Chen et al. [6] and Kort-Kamp et al. [7] studied the electric field distribution in different microstructures and analyzed how the local field increases in grains allowed for higher heating rates and energy absorption. It is important to understand and quantify how local fields in the materials are affected by microstructure and dissimilar constituent properties. In particular, it is important to understand how local field enhancement due to the microstructure and microstructure constituent heterogeneities affect the dielectric breakdown of the materials.

The microstructure-level breakdown process is of interest to engineers who must design components that may be subject to EMP. For example, an engineer designing a power transformer for a region with frequent lightning storms would need to ensure that the dielectrics chosen for the transformer will not fail when subjected to EMP from nearby lightning strikes. The breakdown behavior, and more importantly, the breakdown strengths of materials are often studied experimentally. Although experiments can quantify the behavior and allow comparisons, it is costly and time consuming to fully characterize a material over multiple possible situations; in addition, experiments are incapable of yielding insight into the internal responses of materials to an EMP. Further, experiments cannot be performed on materials that do not yet exist and, therefore, are incapable of enabling systematic exploration of the design of new materials. Computational simulations, on the other hand, can allow detailed internal material responses, including the *E*-field, current, heating mechanisms, temperature evolution, and breakdown, to be analyzed. In addition, the analysis can also allow the breakdown strength of the materials to be computationally determined. In this paper, we develop a computational approach for explicitly analyzing the microstructure-level response of heterogeneous materials to EMP. The method may serve as a template for those wanting to computationally evaluate the effect of EMP pulses on their materials of choice. The approach also allows computations to be performed on theoretically designed materials with systematically varying microstructure attributes and constituent properties to enable identification of new materials configurations with desirable properties for specific applications.

The heterogeneous materials considered here have microstructures that include both dielectric and conductive constituents. The models explicitly resolve the microstructure constituent distributions and the properties of the constituents. The focuses are on the *E*-fields and the breakdown process induced by the E1 pulse. Three commonly used materials are chosen for this investigation: KRAFT paper impregnated with mineral oil, polyether ether ketone (PEEK), and Parker Chomerics 1287 (PC 1287) gasket material. KRAFT paper with oil has been widely used as transformer insulation. PEEK is a high-performance engineering plastic with outstanding resistance to harsh chemicals and excellent mechanical strength. PC 1287 is a commercial gasket material that acts as an electrically conductive elastomer.

Material heterogeneities and the transient nature of the EMP cause the *E*-field in the materials to be non-uniform in both space and time. The spatial and temporal variations of the fields are explicitly tracked. A dielectric breakdown criterion for local constituents is developed and used to enable explicit tracking of the dielectric breakdown process in the microstructure. A statistically equivalent microstructure sample set (SEMSS) with multiple random samples is generated for each material to perform analysis of the variations on the material behavior due to microstructure variations. This technique emulates the use of multiple random samples in experiments.

Dielectric and conductive heating are also explicitly resolved. It is found that thermal dissipation and temperature rises are insignificant in all the materials analyzed due to the extremely short durations of the pulses and the dielectric breakdown processes, which are on the order of picoseconds. As a result, the analysis carried out primarily focused on the *E*-field strength in the materials, evolution of the *E*-fields, and the overall dielectric breakdown of the materials analyzed.

Materials and microstructures

The computational models entail explicit resolution of the heterogeneous microstructures of the three materials and the interactions between the microstructure heterogeneities and an incident E1 pulse. Such models can give insight into aspects of the interactions that are difficult to obtain in experiments currently. Although images of material microstructures can be digitized and directly used in simulations in general [8–10], the lack of sufficient number of images for specific materials often and in our case here renders this option impractical. Also, the use of scanned images is only possible for materials already in existence and cannot be done for exploration of material configurations not yet in existence [11]. On the other hand, microstructure models can be computationally generated or designed to capture the primary microstructure attributes observed in experiments [12] as well as track systematic variations in attributes and features not observed in experiments. In this paper, because of the lack of extensive sets of micrographs for the materials of interest and because of the desire to explore trends, microstructure models are generated for each material based on experimental observations. The primary features of focus are constituent size, shape, and volume fractions. In particular, the volume fractions of constituents are varied systematically. To capture the effects of random variations at the microstructure level, statistically equivalent microstructure sample sets (SEMSS) with multiple samples that conform to the prescribed statistical distribution observed experimentally are used. The SEMSS allow uncertainties in the predicted material behaviors to be captured.

KRAFT paper and oil

KRAFT paper consists of multiple layers of wooden fibers which result from processing [13]. Key attributes of the KRAFT paper microstructure include porosity and fiber orientation, both of which affect the macroscopic material properties. The fiber volume fraction ranges from 80 to 20% (therefore, the porosity ranges from 20 to 80%) [14, 15]. The fibers are randomly oriented such that the overall microstructure is commonly regarded as being isotropic in-plane. Analysis of the fibers and

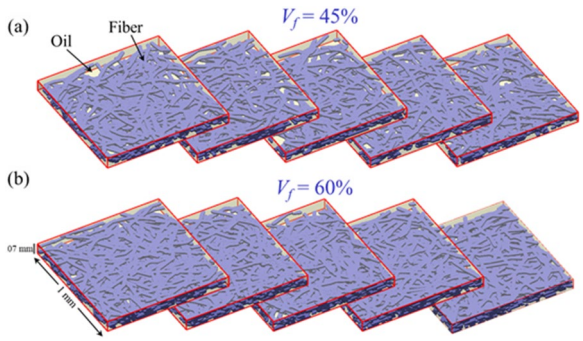

Figure 1: Statistically equivalent microstructure sample sets (SEMSS) for the KRAFT paper and oil composite with fiber volume fractions of (a) 45% and (b) 60%, respectively. Each set has five random samples, allowing the estimation of the range of behavior.

models have been reported. Our model development is based on experimental images from Marulier et al. (see Fig. 2(a) in [15]). The fibers have a maximum length of over 6 mm and an average of 2 mm. The width of the fibers is between 10 and 80 μm with an average of ~ 30 μm. The thickness of the fibers is between 12 and 22 μm [14, 16].

In our model, the pores in the microstructure are filled with Exxon Univolt 60 transformer oil. The computational models for the fiber and oil composite capture key features of the microstructure morphology, size scales, and constituent fractions. The generation of the 3D microstructure models involves random placement of fibers until the desired volume fractions are reached. The fibers have random lengths and orientations and a rectangular cross section of 24 μm × 17 μm. These characteristics conform to the experimentally observed distributions [15] and averages [16]. Although simplifications are involved, the models go beyond models reported in the literature for electrodynamic analyses (e.g., Huang et al. [14]). To analyze the effect of porosity variations observed in experiments [17, 18], two statistically equivalent microstructure sample sets (SEMSS) with two different fiber volume fractions (45% and 60%) are generated, as shown in Fig. 1(a, b). It can be seen that the fibers are randomly orientated in the paper plane, consistent with the experimental image. The regions not occupied by the fibers are filled with oil. Each of the two constituents is assumed to have uniform properties, as reported in [14] and [19], respectively, and shown in Online Resource 1.

PEEK 450G

PEEK is a semicrystalline thermoplastic whose material properties are heavily dependent on its degree of crystallinity. For a polymer, crystallinity is a measure for the amount of aligned polymer chains. The crystalline phase in PEEK is spherulites which are aggregates of polymer chains that form during the solidification process. There can be significant variations in the size, shape, and amount of spherulite regions and amorphous zones within a sample, depending on the curing temperature and the formation process [20]. SEM images (scanning electron microscope) of PEEK 450G containing spherulites from Chu and Shultz (see Fig. 3 in [21]) are the basis of our microstructure generation process. The image shows nearly spherical spherulite particles approximately 2–3 μm in diameter embedded a matrix of base or amorphous PEEK. Spherulite particles are typically radially symmetric spheres with diameters of 2 to 4 μm [21] and have volume fractions of 10–50% [22].

The computational model for PEEK 450G captures the overall characteristics above. The spherulites have a diameter of 4 μm. Five volume fraction levels between 10 and 50% are considered, as shown in Figs. 2(a–e). A SEMSS with five random samples is generated and used for each volume fraction, just like for KRAFT paper and oil. As in the real samples, the particles can be in contact, a result of the growth process. Figure 2(f) shows the number of particles in the samples having a certain nearest neighbor distance for the five SEMSS. The profiles provide a statistical quantification of the distribution of particles relative to each other in terms of the shortest distance between them. Clearly, higher particle volume fractions lead to shorter interparticle distances on average. The primary difference between spherulite particles and the amorphous PEEK matrix in the microstructure lies in their dielectric permittivity. Available data in the literature concerns only the dielectric permittivity of amorphous PEEK and the effective dielectric permittivity of composites of amorphous PEEK and spherulite particles [22], not the permittivity of spherulite. To determine the permittivity of spherulite, the Looyenga equation [23],

$$\varepsilon_{\text{eff}}^{1/3} = \nu_{\text{a}}\varepsilon_{\text{a}}^{1/3} + \nu_{\text{s}}\varepsilon_{\text{s}}^{1/3}, \tag{1}$$

is used. Here, ε_{a} and ε_{s} are the relative permittivities of amorphous PEEK and spherulite, respectively; ν_{a} and ν_{s} are the volume fractions of amorphous PEEK and spherulite, respectively. The value of ε_{s} so determined and the value of ε_{a} are given in Online Resource 2, along with the dielectric breakdown strength E_{bd} and the electrical conductivity for each constituent.

Parker Chomerics 1287 (PC 1287)

Parker Chomerics 1287 (or PC 1287) is a commercial gasket material that comprises a fluorosilicone binder and aluminum microparticles [24–26], which are approximately spherical in shape and typically have a 1 μm thick silver (Ag) coating on their surfaces. As shown in the optical microscope image in Fig. 3(a), the average particle diameter is 80 μm with a standard deviation of ~ 10 μm. The particle volume fraction is 69–70%, and therefore, many particles are in direct contact with each other. Two

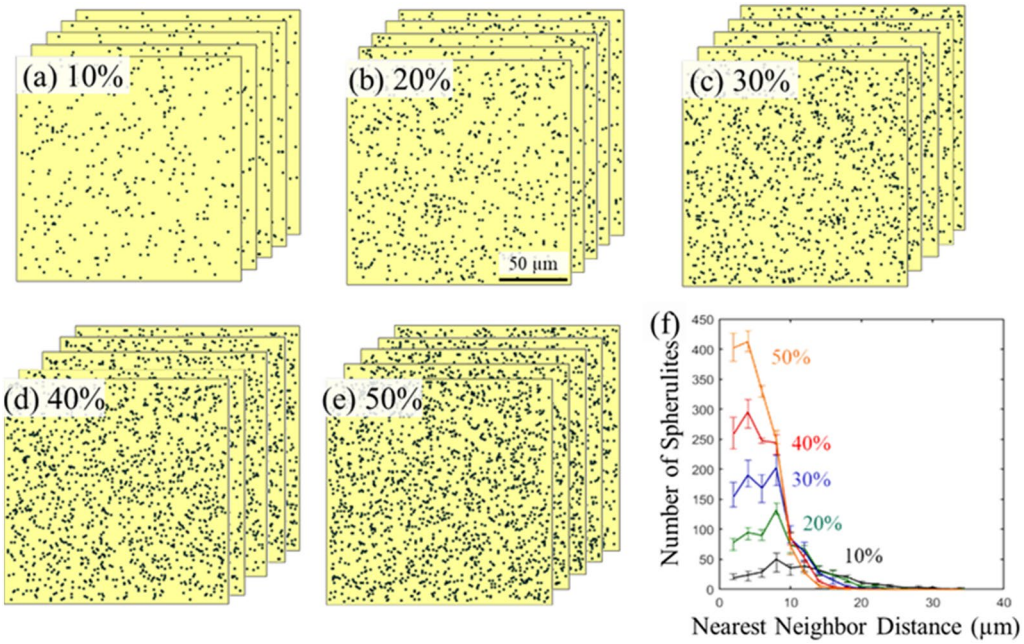

Figure 2: (a–e) SEMSS with five different spherulite volume fractions between 10 and 50%. Each set has five random samples. (f) Statistical distribution of spherulites relative to each other.

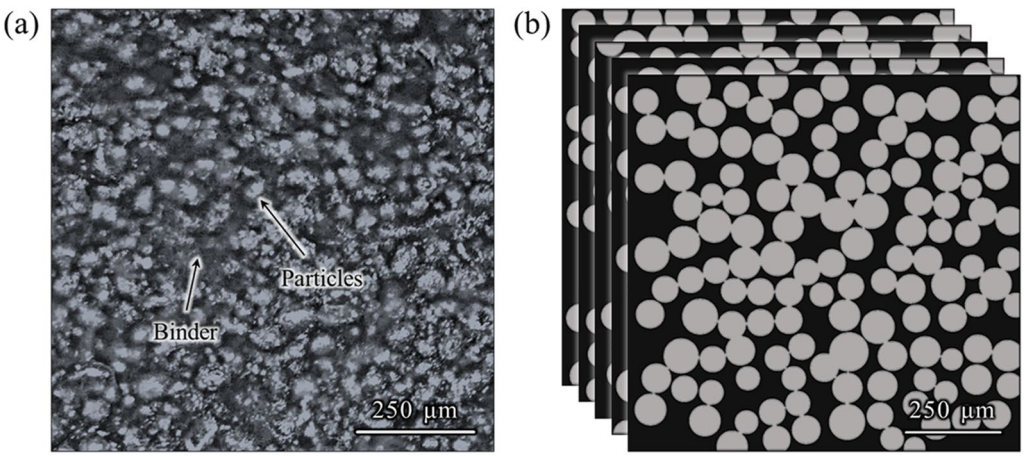

Figure 3: The microstructure of PC 1287 with silver-coated aluminum particles embedded in a fluorosilicone binder. (a) Optical microscope image and (b) computationally generated SEMSS with five random microstructures. Additional SEM images can be found in Online Resource 4.

SEM images of the fracture surfaces of the materials are shown in Online Resource 4, further revealing the size and shape of particles. The overall characteristics are consistent with reports in the literature (e.g., [27]) and the statistical information provided by the vendor.

To capture the overall characteristics described above, a set of microstructure models with five random samples are generated (see Fig. 3(b)). The models explicitly resolve the Al particles, the fluorosilicone binder, and the Ag coating around the particles. The properties of the particles, the binder, and the coating as reported in [28, 29], and [30], respectively, are listed in Online Resource 3.

Results and discussions

KRAFT paper and oil

The electric field distribution within the five equivalent samples with 45% volume fraction of KRAFT paper fiber and oil is shown in Online Resource 8. The fiber has a much higher permittivity than oil (2.4 vs. 6), causing the electric field levels in the

fiber to be lower relative to those in the oil. The highest field level is located near the interface between the fiber and oil. This local increase in the electric field affects where breakdown initiates. The applied peak pulse intensity $E_0 = 50$ kV/m. No breakdown is induced at this applied pulse intensity. The material heterogeneities affect the level of electric field level experienced by the constituents. The highest electric field level in the fibers is 0.89 times the peak pulse intensity due to the fact that the fibers have higher permittivity than the oil. On the other hand, the highest electric field level in the oil is 1.9 times the peak intensity of the applied pulse. However, because the oil's breakdown strength is much higher than that of the fibers (51 vs. 60 MV/m), breakdown occurs in the fibers, not the oil, as discussed later.

To observe and analyze breakdown, the applied peak E-field intensity E_0 is increased successively, until breakdown occurs. The electric field distribution within the KRAFT paper fiber and oil microstructure of one specimen (#1 in Fig. 1) at different times around breakdown occurrence can be seen in Fig. 4(a–c). The applied E-field intensity E_0 is 37 MV/m and the post-breakdown conductivity for the fiber is taken as 10^3 S/m. Breakdown initiates at approximately 4840 ps, which corresponds to the arrival of the peak pulse intensity E_0 for the pulse described in Eq. [2]. The breakdown process is also shown in Fig. 4(d–f) using the evolution of the electrical conductivity. The breakdown process initiates at the fiber/oil interface and propagates into the rest of the material. The breakdown process, from initiation to completion, can happen over a very short time frame, less than 100 ps [1].

Each paper and oil microstructure sample in each of the two SEMSS in Fig. 1 are subjected to E1 pulses with successively higher peak pulse intensity (E_0) levels between 32 and 50 MV/m in order to determine the threshold for breakdown. Breakdown is considered to occur after more than 1% of the total microstructure has become conductive, and the minimum E_0 value of the incoming pulse required to achieve this outcome considered the critical pulse intensity (E_{cr}) required to cause breakdown of the sample and is taken as the breakdown strength of that microstructure sample. This quantification is shown in Fig. 5. In Fig. 5(a), no breakdown occurs as the constituent breakdown strength is artificially set at a very high level intentionally to explore the behavior for comparison. In Fig. 5(b), the constituent breakdown strength is set to their values in Online Resource 1, and the post-breakdown conductivity σ_{bd} is 10^3 S/m. The breakdown strength (E_{cr}) for each microstructure can be clearly identified in Fig. 5(b). The predicted breakdown strengths for each volume fraction of fiber and at different conductivity levels are shown in Table 1 in the conclusions section of this paper. The general trend is that the microstructures with the 60% fiber volume fraction has lower breakdown strengths (34.25–36.25) than those with 45% fibers (34.5–37). Experimental results for KRAFT paper submerged in oil are around 50 MV/m [31]. The calculated ranges are lower than experimental, but aspects including variations in the assumed breakdown strength of the oil and the effect of the liquid could affect the results. Overall, the post-breakdown conductivity σ_{bd} in the range of 10–10^5 S/m does not significantly affect the calculated behavior or material breakdown strength. This is a positive trend and gives more credence to the model results, as the true local constituent σ_{bd} value is not experimentally available currently.

PEEK 450G

The five levels of crystallinity of PEEK 450G between 10 and 50% in Fig. 2 have been studied. Figure 6 displays the effect of

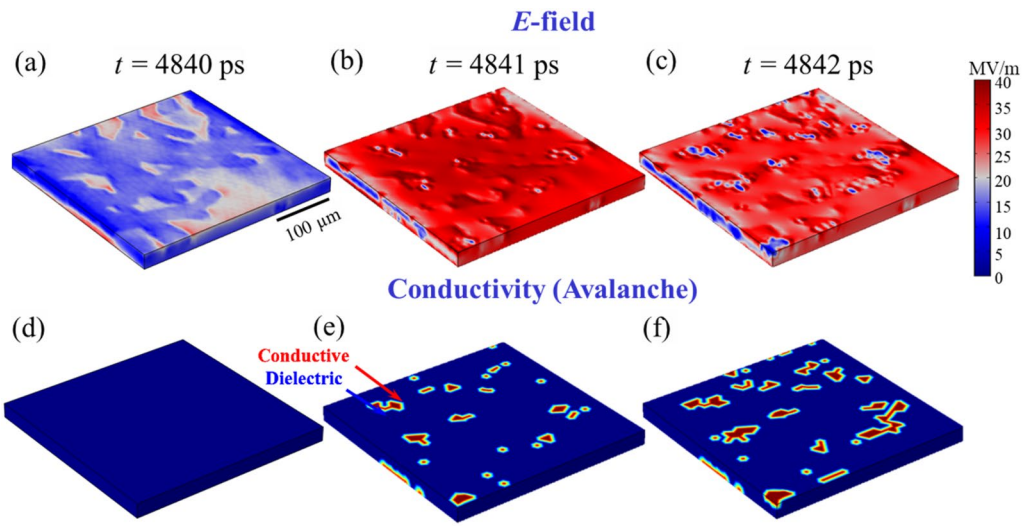

Figure 4: Electric field and conductivity changes in one KRAFT paper and oil specimen (sample #1 in Fig. 1) during the breakdown process. The applied E-field intensity E_0 is 37 MV/m and the post-breakdown conductivity for the fiber is 10^3 S/m.

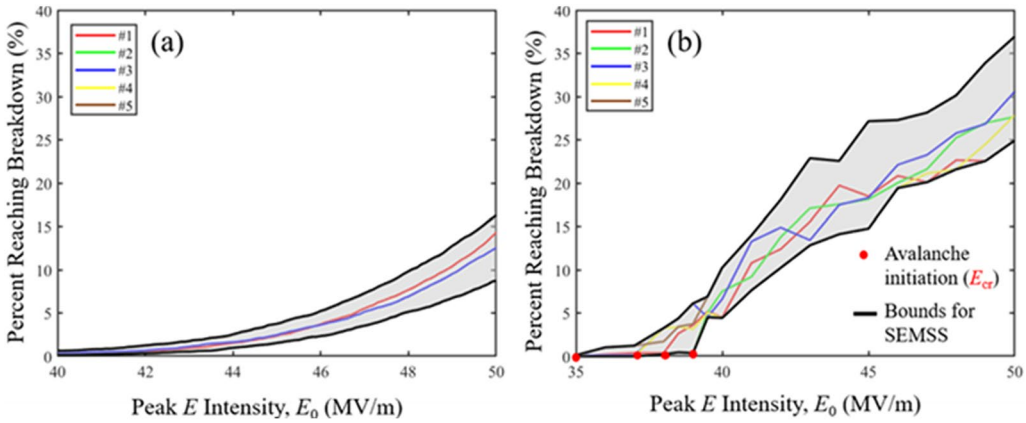

Figure 5: The fraction of material reaching E_{bd} for (a) when breakdown is not modeled and (b) when breakdown is modeled. The post-breakdown conductivity σ_{bd} is 10^3 S/m.

TABLE 1: Critical E1 pulse intensity required for breakdown avalanche (E_{cr}) [MV/m].

	$\sigma_{bd} = 10^1$ S/m		$\sigma_{bd} = 10^3$ S/m		$\sigma_{bd} = 10^5$ S/m	
Material	Range	Average	Range	Average	Range	Average
Paper and oil (45% fiber)	34–35	34.5	35–38	36.5	36–38	37
Paper and oil (60% fiber)	34–34.5	34.25	34–36.5	35.25	35–37.5	36.25
PEEK 450G (20% spherulite)	36.4–36.6	36.5	37–37.6	37.3	34–36	35
PEEK 450G (40% spherulite)	36–37.4	36.7	37–37.7	37.35	35.4–35.6	35.5
PC 1287	500–2200	1,100	2000–3300	2600	2500–16,000	7900

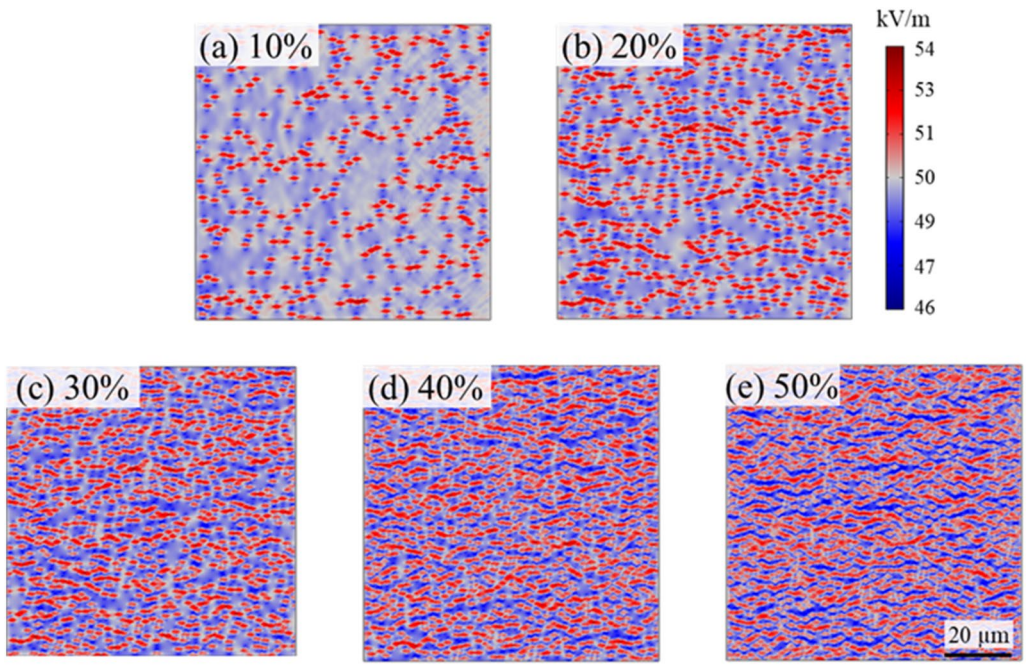

Figure 6: Electric field distributions for different volume fractions of PEEK. The applied pulse peak intensity is $E_0 = 50$ kV/m.

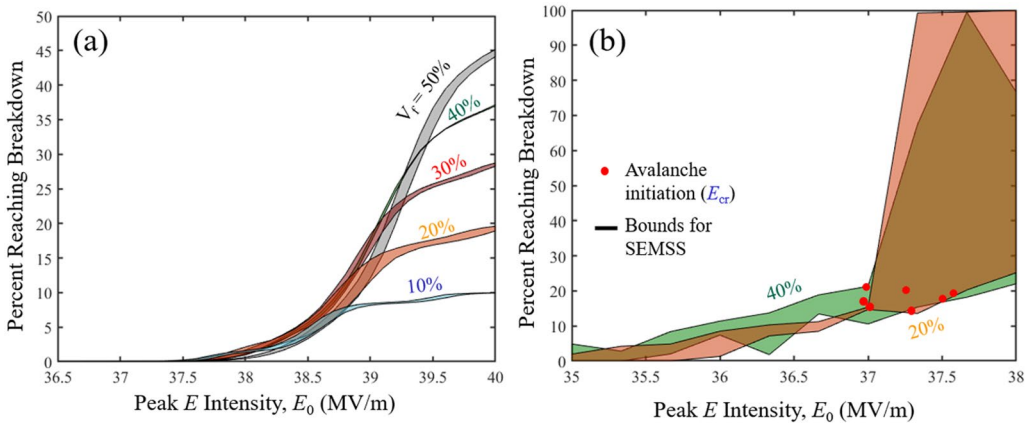

Figure 7: The fraction of a material reaching E_{bd} for (a) when breakdown is not modeled and (b) when is modeled. The post-breakdown conductivity is $\sigma_{bd} = 10^3$ S/m.

increasing the crystallinity of PEEK on the electric field distribution, $\boldsymbol{E}$, when no breakdown occurs ($E_0 = 50$ kV/m). The pulse impinges on the left edge of the samples. Online Resource 9 shows that the overall responses of the five different samples with the same volume fraction of spherulite (30%) are statistically very similar ($E_0 = 50$ kV/m). Therefore, we use the five samples in each set to quantify the statistical range of behavior but use one sample at each volume fraction level for trend identification. In general, spherulites have higher electric field levels than the base PEEK in a microstructure because the amorphous base PEEK has a real relative permittivity ε_r of 3.8 and spherulite has a real relative permittivity ε_r of 3.1. As such, breakdown initiates at spherulites but may propagate through the base PEEK, since spherulite particles may be isolated and not connected. To put in perspective, as the crystallinity increases from 20 to 40%, the highest E-field in spherulites increases from 55.2 to 56.4 kV/m, showing that the peak electric field magnification is around 1.1 times that of the applied field amplitude for both volume fractions. The average E-field in base PEEK decreases from 49.2 kV/m, with an applied field ratio of 0.98, to 45.9 kV/m, with a ratio of 0.92. Volume fraction has a more significant effect on the reduced field in the base PEEK than the highest field in the spherulites, which is the limiting material in the breakdown process.

The breakdown process in PEEK is shown in Online Resource 10 for a sample with a crystallinity of 10%. The applied E-field intensity is $E_0 = 36$ MV/m. It can be seen that breakdown initiates at spherulite particles or clusters of spherulite particles and propagates through both spherulite particles and base PEEK. The effect of breakdown on the electric field can be seen in Online Resource 10(a–d), and the resulting conducting paths can be seen in Online Resource 10(e–h). Each sample is subjected to successively higher pulse intensities between 34 and 45 MV/m. The same process of determining the breakdown strength as that used for the KRAFT paper and oil is used, as shown in Fig. 7, which compares the fraction of each microstructure with E-field levels at or above the constituent breakdown strengths with (Fig. 7(a)) and without breakdown (Fig. 7(b)). The statistical range of the breakdown strengths so obtained is shown in Table 1. The average breakdown field strength shows only a weak dependence on post-breakdown conductivity, increasing from 36.6 to 37.3 MV/m when the conductivity is increased from 10 S/m to 10^3 and decreases from 37.3 to 35.25 MV/m when the conductivity is further increased from 10^3 to 10^5 S/m. More analyses are needed in the future to ascertain the trend, including increasing the number of statistically similar microstructure samples and the levels of the post-breakdown conductivity. Overall, the result here appears similar to what is seen for the fiber and oil composite in that there is no significant effect of the post-breakdown conductivity σ_{bd} on the material breakdown strength. Also, the breakdown strengths for PEEK appear to be similar over the range of spherulite volume fractions analyzed. This perhaps suggests that the breakdown strength is more initiation dominated. When compared to experiments performed by Giants [22], calculated values are ~ 10 MV/m lower than the experimental values, 38 vs 47 MV/m. The experimental trend in the effect of crystallinity on breakdown is shows a decrease from 48 MV/ at 15% crystallinity to 43 MV/m at 35% crystallinity. There is overlap in the experimental calculation so the effect of varying degrees of crystallinity does seem to have less of an effect vs a sample of amorphous PEEK. More analyses are needed to further understand the mechanisms. Note that the focus of this paper is on the development of a means to predict the breakdown strength, not on the analysis of the breakdown process.

Both PEEK and fiber and oil are dielectric composites made up of two different non-conductive constituents. Understanding how these constituents individually affect

the breakdown strength of the overall composite can lead to understanding that facilitates the design of more breakdown-resistant materials. On a relative basis, the overall breakdown strength of PEEK shows less variations in the range of crystallinity considered when compared to the overall breakdown strength of the KRAFT paper fiber and oil dielectric composite over the range fiber volume fraction analyzed. In the fiber and oil composite, each constituent can enhance the breakdown strength of the overall composite. Specifically, the fibers have a low local breakdown strength, but a high permittivity, resulting in a lower local field, as shown earlier. The oil is the opposite, with a very high local breakdown strength, but low permittivity. The electric field in the oil is higher, but not high enough to approach its breakdown strength before the *E*-field in the fibers reach the fiber breakdown strength. In contrast, spherulites are the limiting factor in PEEK as both of its breakdown strength and permittivity are lower compared with those of base PEEK. The highest *E*-field level in the spherulites is 1.1 times the peak intensity of the applied pulse due to the fact that its permittivity is lower than that of the base PEEK. In this sense, the addition of spherulites is a negative on the breakdown strength of the overall PEEK, as they act as initiation sites for breakdown. This is in contrast to the presence of oil in the fiber-oil composite, as oil clearly enhances the breakdown resistance of the fiber from ~ 3 MV/m in air to ~ 37 MV/m.

Parker Chomerics 1287

The electric field ($|\boldsymbol{E}|$) distribution is shown in Online Resource 11 for the five statistically equivalent microstructure samples. The samples are randomly generated with a prescribed mean and standard deviation of particle diameter, as quantified in Fig. 3. Here, a low pulse intensity $E_0 = 50$ kV/m is applied along the left surface such that the microstructure would not experience local dielectric breakdown ($E_{bd} = 80$ MV/m for the fluorosilicone binder). The random variations in microstructural heterogeneities (i.e., the arrangement of the particles) among the samples cause the *E*-field distribution to be non-uniform. Densely packed chains of conductive Ag/Al particles provide electrical shielding along large portions of the microstructure. Hence, the *E*-field magnitude in the binder is very low, with the highest local *E*-field being limited to just ~ 0.01 times the peak pulse intensity. This greatly enhances the breakdown resistance of the overall material, as discussed later.

In Online Resource 12, the current density ($|\boldsymbol{J}|$) distribution is shown for the five samples. Owing to their electrical conductivity, the Ag/Al microparticles have current densities several orders of magnitude higher than those in the fluorosilicone binder. The spatial variations of the current density can be clearly seen. Regions fully enclosed by the closely packed particles experience low current densities due to electrical shielding.

In Fig. 8, the distributions of the electric field, current density, and electrical conductivity are shown for a microstructure

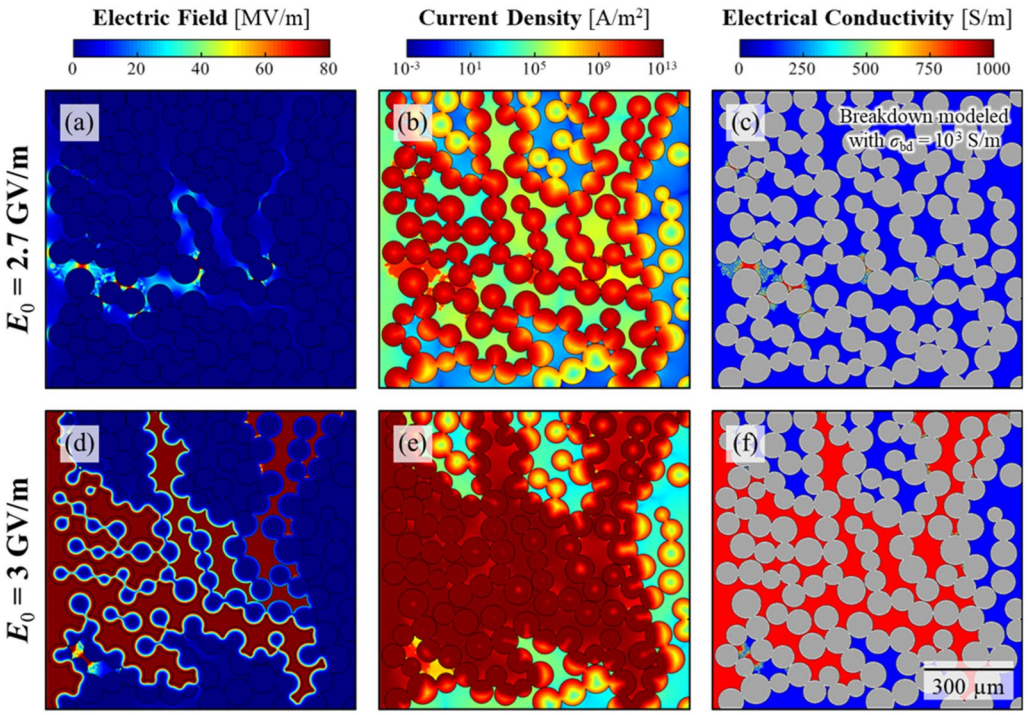

Figure 8: Electric field, current density, and conductivity distributions for the PC 1287 microstructure shown in Fig. 3(a) under applied pulse intensities of (a–c) 2.7 and (d–f) 3 GV/m.

subjected to a high pulse intensity of $E_0 = 2.7$ GV/m. This pulse intensity causes the binder to experience local dielectric breakdown. Breakdown is seen in only a small fraction of the fluorosilicone binder, as indicated by the electric conductivity map in Fig. 8(c). In contrast, at a higher pulse intensity $E_0 = 3.0$ GV/m, a much larger fraction of the binder experiences dielectric breakdown, as seen in Fig. 8(f).

The distributions of the electrical conductivity in Online Resource 13 for the sample shown in Fig. 3(b) under different pulse intensities can be used to visualize the development of breakdown avalanche. For $E_0 = 1.8$–2.7 GV/m (Online Resource 13(a–d)), breakdown is rather localized and the fraction of the binder experiencing breakdown increases only gradually. Avalanches with widespread breakdown are observed when $E_0 \geq 3.0$ GV/m (Online Resource 13(e–f)). There appears to be a critical pulse intensity $E_0 = E_{cr}$ above which avalanche develops. This critical pulse intensity ranges between $E_{cr} = 1.8$–3.3 GV/m for different material cases. To facilitate the determination of E_{cr}, the fraction of the fluorosilicone binder in the microstructures above its breakdown strength as a function of applied pulse intensity E_0 is shown in Fig. 9. In Fig. 9(a), breakdown is not modeled; therefore, the fraction of the binder with E-field levels above the breakdown strength increases steadily as the applied pulse intensity increases. Because the post-breakdown conductivity of fluorosilicone is unknown, a parametric approach is taken with the post-breakdown conductivity ranging between $\sigma_{bd} = 10$–10^5 S/m. In Fig. 9(b–d), breakdown is modeled with the successively higher post-breakdown conductivity (σ_{bd}) values. The plots show the fraction of the binder that has experienced breakdown as a function of the intensity of the applied pulse. The onset of avalanche shown in Fig. 9(b–d) is associated with the rapid spike in the curves and indicated by a red circular symbol on each curve. The applied pulse intensity at this point is taken as the critical pulse intensity E_{cr}. For each value of σ_{bd}, the microstructural heterogeneity fluctuations among the samples cause the critical pulse intensity E_{cr} at which avalanche occurs and which is taken as the breakdown strength of each microstructure to vary significantly. Higher post-breakdown conductivity (σ_{bd}) values correspond to higher E_{cr}. For example, E_{cr} is between 0.4 and 2.1 GV/m for $\sigma_{bd} = 10$ S/m for the five microstructures examined and is 2–15 GV/m for $\sigma_{bd} = 10^5$ S/m. Higher post-breakdown conductivity delays the formation of the avalanche and increases the overall breakdown strength E_{cr} of the composite. Overall, the range of variation of E_{cr} is wide, suggesting that the development of avalanche is very sensitive to microstructure randomness. This means that there is a need for

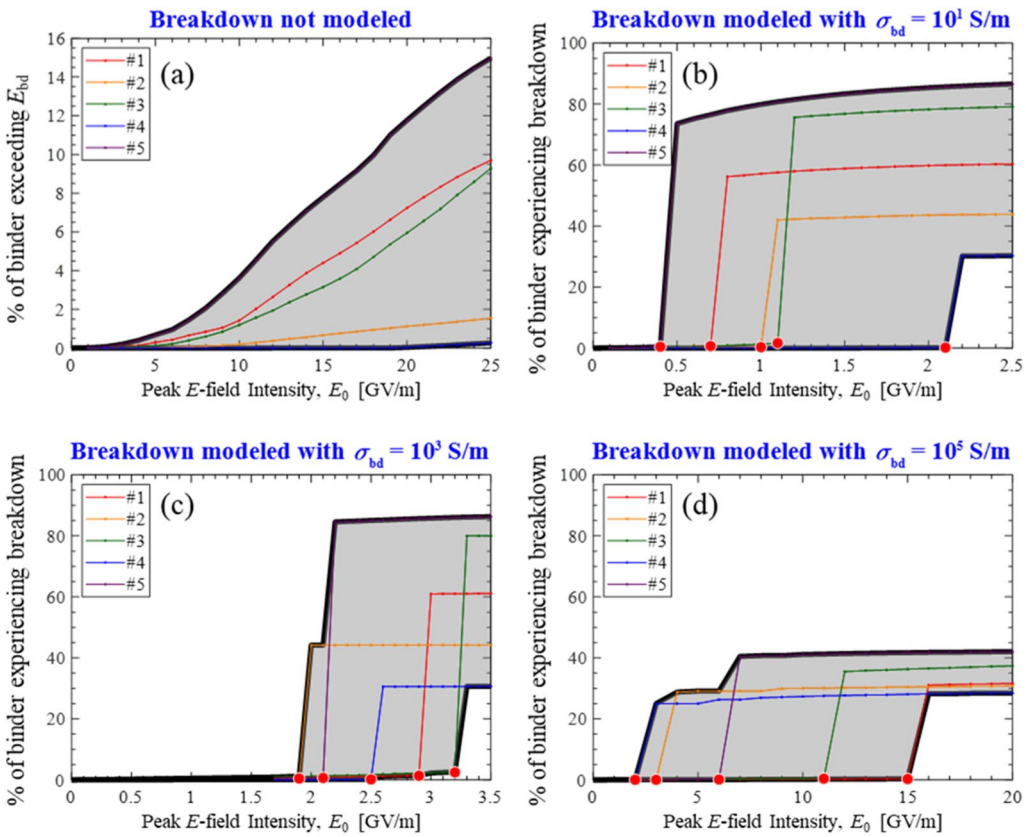

Figure 9: Extent of breakdown in the fluorosilicone binder due to a range of peak E-field intensity for (a) with breakdown not explicitly modeled and (b–d) various values of post-breakdown conductivity.

using a larger number of random samples in the analyses which is not pursued here, as the objective of the current effort is to develop a framework for capturing the microstructure response of materials and an approach for predicting the breakdown behavior. Future work can also focus on the development of material microstructure and behavior uncertainty quantification (UQ), similar to what is pursued for other materials [32].

Summary and conclusion

Dielectric breakdown is an important event for materials in high-voltage situations. Microstructure significantly affects the breakdown behavior and breakdown strength of a material. Understanding when a heterogeneous material whose microstructure consists of two or more constituent components reaches its breakdown strength is an important task in assessing the resilience of important infrastructure and devices. The value of the breakdown strength of such a heterogeneous material is a fundamental and required engineering parameter. Microscale modeling, which explicitly resolves microstructure and microstructure interactions with applied EMP, can enable in-depth understanding and design of materials for increased resilience. In this paper, a methodology that includes a computational model and simulation approach has been developed to analyze the responses of heterogeneous materials with dielectric and conductive constituents to incoming EMP. The framework is used to analyze three commonly used materials. The focus is on the *E*-fields that develop in the microstructures, the development of breakdown avalanche, and the determination of the breakdown strength of the overall materials. The lowest peak intensity of the applied pulse that causes the breakdown avalanche is taken as the breakdown strength of a microstructure sample. The use of multiple statistically equivalent microstructure samples allows the variations of the breakdown strength to be analyzed, just like in experiments and could be used to derive probability distributions describing the breakdown. Although a range of the overall breakdown strength of each of the materials is established, the number of random samples used is relative low; therefore, the range should only be taken as a reference. Further analyses with significantly larger number of samples (e.g., up to 20) should be pursued. Such analyses [33, 34] can also lead to systematic uncertainty quantifications for both the input (microstructure, constituent properties) and output (predicted breakdown strength).

The results of predicted breakdown strength E_{cr} for the three materials are summarized in Online Resource 14 and Table 1. Material heterogeneities enhance the local *E*-fields in the microstructures of the materials analyzed, causing material breakdown; wherever, the peak intensities of incoming EMP are lower than the minimum breakdown strength of the constituents. In the KRAFT paper and oil, the highest local *E*-field level is approximately 0.89 and 1.9 times the peak pulse intensity (E_0) for the fibers and oil, respectively. In PEEK, the highest local *E*-field level is approximately 0.95 and 1.1 times the peak pulse intensity for the base PEEK and the spherulites, respectively. In PC 1287 gasket material, the highest local *E*-field level in the fluorosilicone binder is approximately 0.01 times the peak intensity of the pulse. This modulation of the *E*-field by microstructure and material heterogeneities causes the overall breakdown strength of the materials to be either lower (PEEK) or higher (KRAFT paper & oil, PC 1287) than that of their "weakest" link constituent (the constituent that actually undergo breakdown when the pulse intensity is sufficiently high). For KRAFT paper and oil, the breakdown occurs in the paper fiber, for PEEK, the breakdown initiates in the spherulites, and for Parker Chomerics 1287 gasket material, the breakdown occurs in the fluorosilicone binder.

The E_{cr} can be significantly influenced by both microstructure and post-breakdown conductivity (σ_{bd}) of the constituents in the materials examined. While only a weak dependence of E_{cr} on σ_{bd} is observed in KRAFT paper & oil and PEEK, a strong dependence is seen for the Parker Chomerics 1287 gasket material. This correlation is due to the fact that the Al particles in the PC 1287 material are conductive and can electrically shield portions of a microstructure, thereby more significantly enhancing or magnifying local *E*-field levels. Finally, it is worth pointing out that there is a need to obtain experimental measurements and validation of the trends obtained here in the future. Overall, the approach developed here can be used for other materials and other EMPs as well.

Model Configuration and Boundary Conditions

The EMP considered is the E1 HEMP (early-time high-altitude electromagnetic pulse) waveform, as it can significantly impact the power grid [35], electronics [36], and other systems. This EMP has a quick rise time and high intensity. The characterization of the E1 HEMP provided in IEC 61000-2-9 [37] is

$$E_0(t) = E_{pk}k\left(e^{-\beta t} - e^{-\alpha t}\right), \text{ with } k \equiv \left(\frac{\alpha}{\alpha-\beta}\right)\left(\frac{\alpha}{\beta}\right)^{\frac{\beta}{\alpha-\beta}} \approx 1.3, \tag{2}$$

where $\alpha = 6 \times 10^8\ \mathrm{s}^{-1}$ and $\beta = 4 \times 10^7\ \mathrm{s}^{-1}$. The corresponding spectrum is

$$\begin{cases} E_0(\omega) = \displaystyle\int_{-\infty}^{+\infty} E_0(t)e^{-j\omega t}\mathrm{d}t = E_{pk}k\frac{\alpha-\beta}{(\alpha+j\omega)(\beta+j\omega)}, \\ \text{with } E_{0,\max} = E_{pk}k\left(\dfrac{\alpha-\beta}{\alpha\beta}\right) \approx 1.517 \times 10^{-3}\ (\mathrm{V/m})/\mathrm{Hz} \end{cases} \tag{3}$$

The pulse shape and spectrum are shown in Online Resource 5.

A peak pulse intensity of $E_0 = E_{pk} = 50$ kV/m is used for no-breakdown simulations. Values between $E_0 = 50$ kV/m–15 GV/m are used in the breakdown analyses, depending on the material and size scale. The critical E_0 value required to cause breakdown is denoted as E_{cr}, and taken as the critical E1 pulse intensity needed for breakdown of each material analyzed. This pulse is used to assess the dielectric breakdown of materials but is not intended to be a characterization of the actual value of the field inside the materials produced by an EMP. An assessment of the effect of an EMP should include the boundary conditions between air and the materials, which were not included in this case.

The governing equations for the transient electromagnetic analysis are the Maxwell's equations:

$$\begin{cases} \nabla \cdot \boldsymbol{E} = \rho_q / \varepsilon_0 \varepsilon_r, \\ \nabla \cdot \boldsymbol{B} = 0, \\ \nabla \times \boldsymbol{E} = -\partial \boldsymbol{B} / \partial t, \\ \nabla \times \boldsymbol{B} = \mu_0 \mu_r \left[\boldsymbol{J} + \varepsilon_0 \varepsilon_r \left(\partial \boldsymbol{E} / \partial t \right) \right] \end{cases}. \tag{4}$$

where $\boldsymbol{E}$ is the electric field, $\boldsymbol{B}$ is the magnetic field, ρ_q is the volumetric free-charge density, $\boldsymbol{J}$ is the current density, and $\varepsilon_0\varepsilon_r$ and $\mu_0\mu_r$ are the permittivity and permeability of the material, respectively. The first and second equations are Gauss's laws for electricity and magnetism, respectively; the third equation is Faraday's law of induction; and the fourth equation is Ampère's law. These equations are solved using the *temw* (Transient Electromagnetic Waves) module in COMSOL. Even though the analysis tracks the development of the magnetic field (B-field) as well as the electric field, the magnetic field has essentially no effect on the response of the materials (electric field induced dielectric breakdown) analyzed here and is, therefore, not discussed in this manuscript.

The incoming pulse is applied to a surface for each material, as shown in Online Resource 6. Due to the complexity of the microstructure for KRAFT paper & oil, a three-dimensional model (3D) model with a second-order transparent boundary condition (B.C.) is used (Online Resource 6(a)). For PC 1287 and PEEK, a two-dimensional (2D) model with lossless and transparent boundary conditions (B.C.s) is used (Online Resource 6(b)). In these models, a lossless boundary reflects the incident electric field. On the other hand, a transparent boundary fully transmits the fields incident upon it. The transparent condition is used to simulate the effects of a perfectly matched layer of material, effectively allowing a region of a much large piece of material to be analyzed in detail.

To simulate the breakdown process in the microstructure, a local breakdown criterion for each constituent is required. The criterion used can be stated as follows:

$$\sigma(\boldsymbol{x}, t) = \begin{Bmatrix} \sigma_0, \text{ if } \max\limits_{t \in [t_0, t]} |\boldsymbol{E}(\boldsymbol{x}, t)| < E_{bd} \\ \sigma_{bd}, \text{ if } \max\limits_{t \in [t_0, t]} |\boldsymbol{E}(\boldsymbol{x}, t)| \geq E_{bd} \end{Bmatrix}, \tag{5}$$

where σ is the current conductivity, σ_0 is the initial conductivity before breakdown, σ_{bd} is the post-breakdown conductivity, and $\sigma_{bd} >> \sigma_0$. Illustrated in Online Resource 7, this criterion implies that breakdown occurs irreversibly at a constituent material point if the local electric field (E-field) intensity reaches or exceeds the breakdown strength (E_{bd}) of that constituent material. Upon onset of breakdown, the material's local electrical conductivity increases irreversibly from its initial low dielectric value (σ_0) to the high post-breakdown conductive value (σ_{bd}). There have been different models for simulating the effects of dielectric breakdown, including the fractal path models [38] and the energy-dependent model [39]. These models focus on the path of breakdown, and do not always account for the effects of conductivity change or resolve the breakdown process. In this paper, the effect of the changing conductivity on the electric field distribution [40] in the material is considered. The sharp rise in conductivity upon breakdown can cause the local electric field and fields elsewhere to change significantly, thereby affecting progression of the breakdown process.

Due to lack of accurate reports of σ_{bd} values, a parametric approach is used in the mesoscale simulations by considering several values of σ_{bd} between 10 and 10^5 S/m. The results, especially the breakdown strength of the overall materials (KRAFT paper and oil, PEEK, and PC 1287) corresponding to each σ_{bd} value, are discussed.

Acknowledgments

The research at Georgia Tech is supported by the Sandia LDRD Program through Standard Purchase Order 2157495. Any subjective views or opinions that might be expressed in the paper do not necessarily represent the views of the U.S. Department of Energy or the United States Government. Sandia National Laboratories is a multi-mission laboratory managed and operated by National Technology and Engineering Solutions of Sandia, LLC, a wholly owned subsidiary of Honeywell International, Inc., for the U.S. Department of Energy's National Nuclear Security Administration under contract DE-NA0003525. The authors would like to thank Dr. Gregory B. Kennedy at Georgia Tech and Dr. Sean Bishop for their assistance in obtaining the micrographs for one of the materials analyzed.

Data availability

The datasets generated during and/or analyzed during the current study are available from the corresponding author on reasonable request.

Declarations

Conflict of interest On behalf of all authors, the corresponding author states that there is no conflict of interest.

Supplementary Information

The online version contains supplementary material available at https://doi.org/10.1557/s43578-022-00763-3.

References

1. S. Glasstone, P.J. Dolan (U.S. Department of Defense, 1977)
2. S. Campione, L.K. Warne, (Sandia National Lab.(SNL-NM), Albuquerque, NM, 2020)
3. B. Conley, P. Henny, N. Erickson, M. Halligan, B. Toby, D. Pommerenke, M. Walker, C. Essary, P. Dixon, D.G. Beetner, IEEE Trans. Electromagn. Compat. **58**(4), 1042 (2016)
4. S.L. Dvorak, D.G. Dudley, IEEE Trans. Electromagn. Compat. **37**(2), 192 (1995)
5. J. Sun, M. Huang, J. Peng, W. Niu, L. Zhang, in Proceedings of the 9th International Symposium on Antennas, propagation and EM theory, (IEEE, 2010), pp. 701
6. M. Chen, M.A. Zikry, M.B. Steer, IEEE Access. **6**, 24596 (2018)
7. W.J.M. Kort-Kamp, N.L. Cordes, A. Ionita, B.B. Glover, A.L.H. Duque, W.L. Perry, B.M. Patterson, D.A.R. Dalvit, D.S. Moore, Phys. Rev. Appl. **5**(4), 044008 (2016)
8. A. Gurumurthy, A.M. Gokhale, A. Godha, M. Gonzales, Metallogr. Microstruct. Anal. **2**(6), 364 (2013)
9. H. Singh, A.M. Gokhale, Mater. Charact. **54**(1), 21 (2005)
10. M. Zhou, A. Needleman, R.J. Clifton, J. Mech. Phys. Solids **42**(3), 423 (1994)
11. U. Roy, S. Kim, C. Miller, Y. Horie, M. Zhou, Modell. Simul. Mater. Sci. Eng. **26**(8), 085004 (2018)
12. Y. Wei, D.H. Olsen, C.M. Miller, K.B. Wagner, A. Keyhani, N. Thadhani, M. Zhou, Multisc. Sci. Eng.. **2**(1), 7 (2020)
13. F.S. Chakar, A.J. Ragauskas, Ind. Crops Prod. **20**(2), 131 (2004)
14. J. Huang, Y. Zhou, L. Dong, M. Huang, Z. Zhou, R. Liu, AIP Adv. **6**(7), 075113 (2016)
15. C. Marulier, P.J.J. Dumont, L. Orgeas, S.R.D. Roscoat, D. Caillerie, Cellulose **22**, 1517 (2015)
16. C. Ververis, K. Georghiou, N. Christodoulakis, P. Santas, R. Santas, Ind. Crops Prod. **19**(3), 245 (2004)
17. S. Borodulina, H.R. Motamedian, A. Kulachenko, Int. J. Solids Struct. **154**, 19 (2018)
18. I. Pulkkinen, V. Alopaeus, Wood Res. Technol. **66**(1), 111 (2012)
19. ExxonMobil, Univolt Transformer Oils. https://www.exxonmobilchemical.com/en/products/transformer-oils. Accessed May 2020
20. B. Crist, J.M. Schultz, Prog. Polym. Sci. **56**, 1 (2016)
21. J.N. Chu, J.M. Schultz, J. Mater. Sci. **25**, 3746 (1990)
22. T.W. Giants, IEEE Trans. Dielectr. Electr. Insul. **1**(6), 991 (1994)
23. L. Jylhä, A. Sihvola, J. Phys. D **40**(16), 4966 (2007)
24. P. Lessner, D. Inman, in 1993 International Symposium on Electromagnetic Compatibility, (IEEE, 1993), pp. 207
25. Y.S. Lin, S.S. Chiu, Polym. Eng. Sci. **44**(11), 2075 (2004)
26. O.R. Pierce, G.W. Holbrook, O.K. Johannson, J.C. Saylor, E.D. Brown, Ind. Eng. Chem. **52**(9), 783 (1960)
27. C.E.G. Design, EMI Shielding Engineering Handbook, Chomerics. Accessed November 2000
28. J.G. Cook, J.P. Moore, T. Matsumura, M.P. Van Der Meer, in Thermal Conductivity 14, (Springer, 1976), pp. 65
29. L.J. Romasanta, M.A. López-Manchado, R. Verdejo, Prog. Polym. Sci. **51**, 188 (2015)
30. J. Xie, S. de Gironcoli, S. Baroni, M. Scheffler, Phys. Rev. B **59**(2), 965 (1999)
31. W. Wu, R. Liao, F. Zhang, L. Yang, in 2012 International Conference on High Voltage Engineering and Application, (IEEE, 2012), pp. 199
32. J.H. Shin, M. Zhou, J. Appl. Phys. **129**(24), 245103 (2021)
33. Y. Li, M. Zhou, Eng. Fract. Mech. **205**, 14 (2019)
34. Y. Li, M. Zhou, J. Mech. Phys. Solids **61**(2), 472 (2013)
35. E. Savage, J. Gilbert, W. Radasky, in Report Meta, (Oak Ridge National Laboratory, Oak Ridge, TN, 2010)
36. W.A. Radasky, in 2010 Asia-Pacific International Symposium on Electromagnetic Compatibility, (IEEE, 2010), pp. 758
37. Electromagnetic Compatibility, in IEC Standard, 1996)
38. L. Niemeyer, L. Pietronero, H.J. Wiesmann, Phys. Rev. Lett. **52**(12), 1033 (1984)
39. Z. Suo, J. Mech. Phys. Solids **41**(7), 1155 (1993)
40. S. Noguchi, M. Nakamichi, K. Oguni, Comput. Methods Appl. Mech. Eng. **371**, 113295 (2020)